Additive Manufacturing 57 (2022) 102962

Contents lists available at ScienceDirect

Additive Manufacturing

journal homepage: www.elsevier.com/locate/addma

Research Paper

Revealing the microstructural evolution of electron beam powder bed fusion and hot isostatic pressing Ti-6Al-4V in-situ shelling samples using X-ray computed tomography

Riccardo Tosi [a,b], Chu Lun Alex Leung [c,d,*], Xipeng Tan [e,**], Emmanuel Muzangaza [a,b], Moataz M. Attallah [a]

[a] School of Metallurgy and Materials, University of Birmingham, B15 2TT Birmingham, United Kingdom
[b] National Centre for Additive Manufacturing, The Manufacturing Technology Centre, Ansty Park, Coventry CV7 9JU, United Kingdom
[c] Department of Mechanical Engineering, University College London, Torrington Place, London WC1E 7JE, United Kingdom
[d] Research Complex at Harwell, Rutherford Appleton Laboratory, Harwell, Oxfordshire OX11 0FA, Oxon, United Kingdom
[e] Department of Mechanical Engineering, National University of Singapore, 9 Engineering Drive 1, Singapore 117575, Singapore

ARTICLE INFO

Keywords:
Additive manufacturing
Hot isostatic pressing
Microstructure
Consolidation
X-ray computed tomography

ABSTRACT

Electron beam powder bed fusion/hot isostatic pressing (E-PBF/HIP), also known as in-situ shelling, is an emerging technology that produces components by only forming their shells whilst retaining sintered powder at the core, and then using HIP to consolidate the entire structure. E-PBF/HIP can boost additive manufacturing productivity, however, the fundamental understanding of the process-microstructure-property correlations remains unclear. Here, we systematically investigate the microstructural evolution of E-PBF/HIP Ti-6Al-4V parts as a function of hatch melting parameters. All HIPped samples achieve full densification, however, their microstructures are significantly different from one another. Using X-ray computed tomography (XCT) and optical microscopy, our results show that the HIPped Ti-6Al-4V microstructure can be controlled by varying the porosity, P (%), pore surface areas and morphology in the as-built parts with a single set of HIP parameters. The HIPped microstructures still exhibit the as-built columnar grains when the as-built porosity, $P < 3$ % with mainly spherical micro-pores; a mixture of columnar and equiaxed grains when the $3\ \% < P \leq 5\ \%$ with a tortuous and interconnected pore network; and equiaxed grains when $P > 5$ % with a highly dense pore network. This work suggests two main drivers for the grain morphology transitions during HIP: (1) a dramatic increase in pore volume increases the localised applied pressure up to 4 times at the core region of the sample and (2) minimise lack-of-fusion pores with high surface energies, promoting dynamic recrystallisation. This study provides a fundamental insight into the E-PBF/HIP technology, showing the feasibility to tailor microstructural properties of E-PBF built parts whilst boosting additive manufacturing productivity.

1. Introduction

Powder bed fusion (PBF) is a mainstream metal additive manufacturing (AM) technology that builds up metallic parts directly from computer-aided design files, layer by layer, with a controlled heat source. Industries have shown great interest in AM technologies due to their ability to produce near-net-shape parts without the use of dies or heavy machining, reducing material waste and lead time [1].

In recent years, electron beam powder bed fusion (E-PBF) has achieved unprecedented success in AM of Ti-6Al-4V for biomedical and aerospace applications [2]. However, it faces a few technical challenges, e.g. the occasional appearance of gas pores, low production rates, and anisotropic mechanical properties owing to the columnar grain structure. It is imperative to deploy post-processing to overcome these barriers for broader industrial applications. Post processing, e.g. hot isostatic pressing (HIP), is often used in casting, powder metallurgy, and metal AM to reduce processing defects, e.g. gas pores, lack of fusion, and cracks, resulting in better microstructural stability and improved mechanical properties [3,4].

Knight and Wright [5] performed one of the earlier studies on

* Corresponding author at: Department of Mechanical Engineering, University College London, Torrington Place, London WC1E 7JE, United Kingdom.
** Corresponding author.
E-mail addresses: alex.leung@ucl.ac.uk (C.L.A. Leung), xptan@nus.edu.sg (X. Tan).

https://doi.org/10.1016/j.addma.2022.102962
Received 8 March 2022; Received in revised form 14 May 2022; Accepted 8 June 2022
Available online 11 June 2022

selective laser sintering (SLS) and hot isostatic pressing (SLS/HIP) techniques. They manufactured shelled samples containing loose powder in the core and subsequently consolidated them under the HIP treatment. The SLS/HIP approach aims to lower the product cost and increase productivity for making replacement parts, though its major drawback is the HIP-induced shrinkage. Qiu et al. [6] adopted the SLS/HIP approach and made Ti-6Al-4V canisters using a laser powder bed fusion (LPBF) system, using the term "in-situ shelling". The LPBF/HIPped microstructure showed a homogenous microstructure at the core-shell interface. However, these canisters were distorted and underwent part shrinkage after HIPping. Similar studies were investigated in which the L-PBFed canister parts encapsulated gas atomised powder [7–10]. After HIP, the core of samples exhibits a high quantity of residual pores and this is possibly due to the gas transfer from the gas atomised powder or gas entrapment from the processing atmosphere.

To avoid gas entrapment during AM, Leicht et al. [11] fabricated Ti-6Al-4V hollow cube structure using E-PBF which operates in vacuum. They found that a hollow cube with a shell thickness below 1 mm can cause surface leaks and subsequently rupture during HIPping. Frisk et al. [12] revealed that the core of the E-PBF/HIPped Ti-6Al-4V samples exhibited equiaxed prior β grain microstructure, a homogenous microstructure at the interface of the core-shell materials, and negligible porosity, though, shrinkage was evident in these parts. The E-PBF/HIP approach shows great potential to achieve a non-conventional (or non-epitaxial) microstructure typically found in AM [13], however, none of the prior studies explain the underlying microstructural evolution mechanisms in E-PBF/HIP.

In summary, the HIP-assisted AM technology has moved from SLS/HIP to L-PBF/HIP and E-PBF/HIP, which partially minimises process-induced porosity. All these HIP-assisted AM techniques only require forming the shell of the part with a core region containing partially consolidated loose powder, which significantly reduces the layer melting time and enhances the manufacturing productivity. To unlock the true benefits of E-PBF/HIP, we must better understand the effects of process parameters and the physics that govern the as-built and HIP microstructure. Here, we assess the E-PBF/HIP manufacturing technology using a systematic experimental approach and materials characterisation techniques. We quantify the effects of process parameters on the shrinkage, density, microstructure, and mechanical properties of the parts as well as their manufacturing time.

2. Experimental procedures

2.1. Parts and build file preparation

For this study, the Arcam A2XX electron beam melting (EBM) system (GE Additive, USA) was used to fabricate as-built samples which have a fully melted shell and a core region with sintered powder. The control software used for the A2XX system is EBM Control 3.2 [14]. E-PBF samples were made with pre-alloyed Grade 5 Ti-6Al-4V powder (GE Additive, USA) with a size range of 45–106 μm. For each of the 16 build conditions, we built four samples (a total of 64 specimens). The shell of the as-built samples was manufactured using the ARCAM standard contour melting scheme whereas the core region of the samples underwent different hatching parameters, e.g., beam focus offset (BF) and speed functions (SF), see Table 1. A detailed definition of BF and SF can be found elsewhere [14,15]. The samples made by theme #16 did not involve hatching, i.e. their core region contained semi-sintered powders.

Fig. 1(a) shows a CAD image of the as-built can which has a height and a diameter of 15 mm, and a shell thickness of 1.5 mm. In addition, 4 identical Ti-6Al-4V blocks ($20 \times 20 \times 100$ mm^3) were fabricated with the lower half of full-density material using Arcam standard setting (theme #6 in Table 1), and the upper half was a shell containing sintered powder, see Fig. 1**(b).** All 4 samples were processed with HIP for densification. One of the samples was used for microstructural analysis and the remaining three samples were machined into ASTM E8 test pieces to ensure minimal repeatability of tensile data (comply with the ASTM-F2924 standard). The sample build positions and orientations are shown in Fig. 1**(c–d).** All samples had the same customised support structures located on their bottom surface, see Fig. 1**(e).**

To maintain the shell thickness at ~ 1.5 mm when processing with different hatching parameters, we increased the number of contour lines [16] from 2 to 5. The shell thickness was selected based on Leicht et al. [11] study to prevent surface leaks and rupture, in addition, the internal and external rounded corners were designed to accommodate shrinkage during HIPping. The HIPping process was performed at Hauck Heat Treatment Ltd (TTI), with a constant argon gas pressure of 103 MPa, a temperature of 920 °C, and a holding time of 2 h. The as-built sample design also allows tracking of the manufacturing time using Materialise Magics® software and the machine log file. Here, the combined effects of BF and SF on the microstructure before and after HIP are investigated, as they alter the energy density delivered during melting and the overall manufacturing time.

2.2. Hatching parameters and machine settings

The volumetric energy density, ***E***, imparted to the powder bed during hatching was calculated by: $E = Q/(d * t)$ where the amount of linear energy density, $Q \quad (\mathrm{J/mm}) = (A * V)/v$, A is the beam current (mA), V is the acceleration voltage (kV), v scan speed (mm/s), d is the hatching space (mm), and t is the layer thickness (mm). We used a nominal 18 mA beam current, 60 kV acceleration voltage, 0.2 mm hatching space, and 70 μm layer thickness, similar settings can be found in Refs. [15,17–19]. Table 2 shows an increase in *SF* would increase the v but decrease in Q and E.

2.3. Post analysis procedure

After manufacturing the specimens, all bottom supports were removed. An as-built sample per condition was vertically sectioned along the *x-z* plane for an initial porosity assessment using optical microscopy (OM). We also performed Archimedes measurements, micro-hardness tests, and microstructural analysis by OM and scanning electron microscopy (SEM) on both as-built and HIP specimens to better understand their densification, microstructure, and mechanical performance. Micro-hardness measurements were made before and after the HIP treatment at the core region of the specimens using a Buehler MicroMet 6030 (500 g load and 15 s dwell time) in the x-z/y-z plane, where the reported value is based on an average of nine equidistant 1 mm indents. Tensile tests were conducted at a strain rate of 2.5×10^{-4} s^{-1} using the ASTM E8 coupons at room temperature.

2.4. X-ray computed tomography (XCT)

Based on the 2D porosity quantification and the resultant microstructure before HIPping, we selected key samples to be scanned by X-ray computed tomography (XCT) to study the volume and surface area of internal pores. The selected samples were produced using themes #1,

Table 1
Themes used during the experiment. (*) Arcam standard settings.

Theme	#1	#2	#3	#4	#5	#6	#7	#8	#9	#10	#11	#12	#13	#14	#15	#16
Speed function (SF)	26	26	26	26	26	36*	36*	36*	36*	36*	46	46	46	46	46	N.A.
Beam focus offset (BF)	0	9*	19	29	39	0	9*	19	29	39	0	9*	19	29	39	N.A.

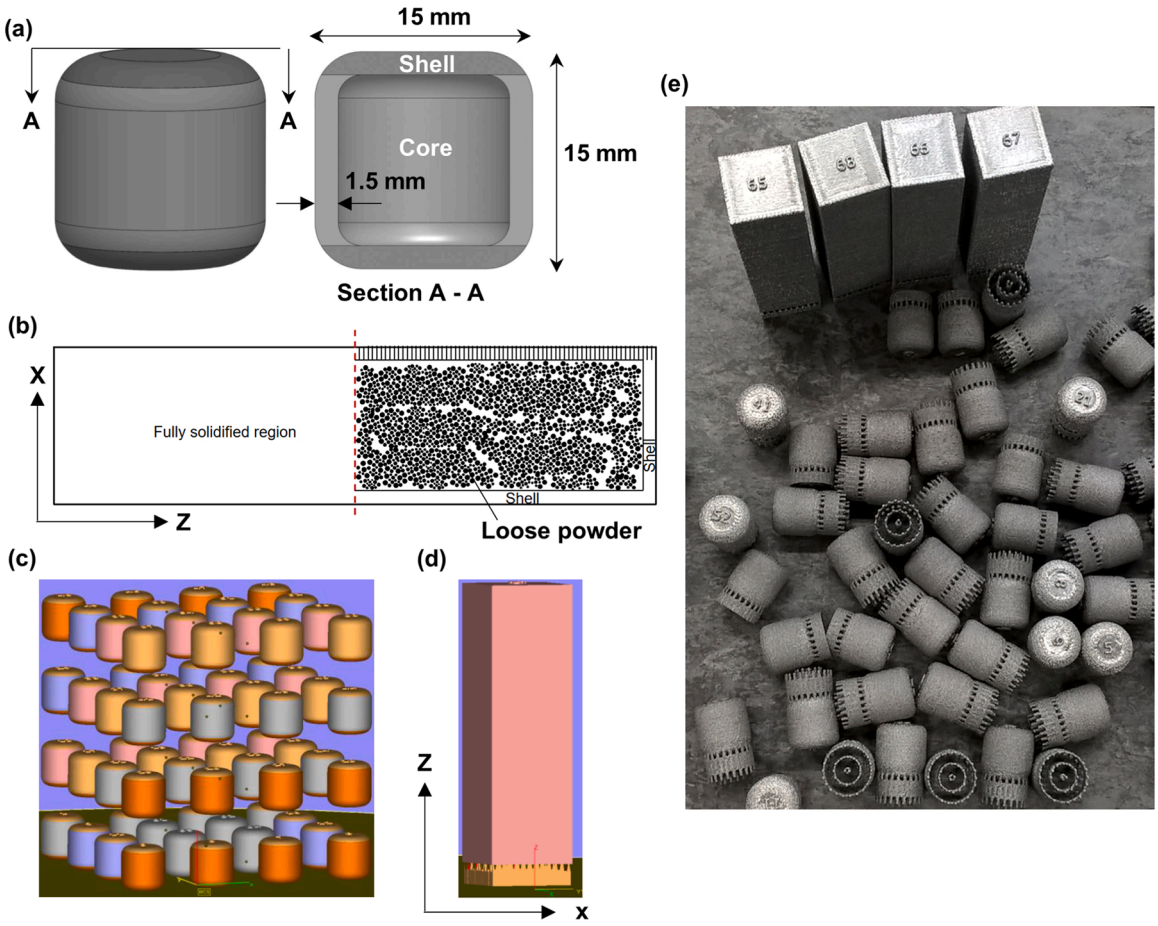

Fig. 1. (a) CAD drawings of the as-built samples and (b) four tensile bars were made by encapsulating powder from the middle to the top region. (c) Images taken from Materialise Magics® showing the orientation and position of (a) Ti-6Al-4V as-built and (d) tensile samples in the same build file, where each colour shows different theme settings; (e) images of the as-built specimens with support structures.

Table 2
SF variables as a function of scan speed (v), linear energy density (Q), and volume energy density (E).

SF	Scan speed, *v* (mm/s)	Linear energy density, *Q*, (J/mm)	Volumetric energy density, *E* (J/mm^3)
26	1529	0.7	50.5
36	2094	0.5	36.8
46	2659	0.4	29.0

#5, #8, #9, #10, #14, and #15 (see Table 1), and they were scanned using the XT H 450 micro-focus XCT system (Nikon metrology UK Ltd., UK) located at the Manufacturing Technology Centre, UK. Each XCT scan was performed at 115 kV and 82 μA with a 0.5 mm Cu filter, comprising 1760 radiographic projections with a 2 s exposure time per projection. All XCT scans were reconstructed using filtered back projection and beam hardening correction algorithms embedded in CT Pro3D (Nikon, UK). The voxel size of the reconstructed volume was $10.8 \times 10.8 \times 10.8$ μm^3 and the minimum resolvable pore size requires > 5 voxels, which is equivalent to 22.9 μm.

2.5. Image processing, porosity quantification, and data visualisation

The reconstructed image volumes were post-processed and quantified using Avizo 2019.2 (Thermo Fisher Scientific, USA) and the 3D porosity analysis was performed following a standard procedure outlined in [16]. We quantified the pore volume, porosity (%), and surface area to study their effects on the resultant microstructure after HIPping. We selected a region of interest of $500 \times 500 \times 500$ voxels (or $5.4 \times 5.4 \times 5.4$ mm^3) at the core of the sample to visualise the pore morphology in 3D.

3. Results and discussion

3.1. Influence of process parameters on porosity

The as-built samples were first analysed by OM to investigate the effects of processing themes on the microstructure, such as grain morphology and pore features. All samples with a BF of 0, 9, and 19 displayed a porosity of < 0.15 %, which is relatively low for E-PBFed parts. Increasing SF will lead to a decrease in linear energy density, *Q*, during E-PBF. A low Q promotes the formation of lack-of-fusion pores in the E-PBFed part [15,16,20–22], see result summary in Table 3.

Table 3 shows that sample #7 (standard settings) yields a porosity of

Table 3
2D OM quantification of porosity (%) in the core region of the as-built samples (rounded to 1 d.p).

Process parameter	Porosity, *P* (%) (Sample #) Speed Function, SF		
Beam Focus, BF	SF26	SF36	SF46
BF0	0.1 (#1)	0.1 (#6)	0.1 (#11)
BF9	null (#2)	0.2 (#7)	0.1 (#12)
BF19	0.2 (#3)	0.3 (#8)	0.3 (#13)
BF29	0.2 (#4)	10.1 (#9)	21.0 (#14)
BF39	15.0 (#5)	17.7 (#10)	30.8 (#15)

0.15 %. The samples with low porosities were made by themes #1, #2, #6, #11, and #12 where a sufficiently high volumetric energy density electron beam was used for melting. Samples made by themes #8 and #13 had the maximum P of 0.3 % using a BF < 29. Samples made by themes #5, #9, #10, #14, and #15, with a low input volumetric energy density had a $10\ \% < P < 30\ \%$, which is not suitable for high-performance applications according to the ASTM aerospace standards [23].

Fig. 2 shows the optical micrographs of samples #1, #5, #8, and #15 before and after HIP. Samples #1 and #8 show that the spherical pores are randomly distributed in both core and shell regions. The low BF setting gives a high volumetric energy density, promoting good fusion between layers of materials, and hence their $P = 0.1$ % and $P = 0.3$ %, respectively. When $P < 0.3$ %, the resultant microstructure of the post HIP samples only exhibits columnar grains. In contrast, samples #5 and #15 show a high volume percentage of large irregular pores that are interconnected and many pores are present near the shell region. The high porosity can be attributed to the turning function [24] during hatching and the high v further reduced the volumetric energy density for E-PBF in the edge area. Tammas-Williams et al. [24] explained that the tunnel defects are usually located in the turning region and below overhanging features owing to insufficient imparted energy. After HIPping, all pores are closed and the samples are fully dense.

Given that all samples underwent the same HIP parameters, our results show that the resultant HIPped microstructure depends highly on porosity in the as-built samples, such that the grain morphology was evolved from fully columnar ($P < 0.3$ %) in sample #1 to the columnar and equiaxed mixture ($0.3\ \% < P < 15\ \%$) in sample #5 and then fully equiaxed grains ($P > 15$ %) in sample #15. Besides the porosity, we hypothesise that the pore characteristics may influence the heat transfer and localised deformations during HIPping, and hence altering the HIPped microstructure, see discussion later.

3.2. 3D quantification of as-built porosity

To further understand the effect of pore characteristics on the HIP process and resultant microstructure, we examined the pore structure inside E-PBF as-built samples in 3D using XCT. Fig. 3**a–c** show virtual orthoslices (*x-y*, *y-z*, and *x-z planes*) of samples #8, #5, and #15 and their corresponding pore features in 3D (Fig. 3**d–f**). The XCT rendered images display that most pores located in the core of sample #8 are spherical rather than interconnected, corroborating with the OM results in Fig. 2. In contrast, the 3D rendered results of samples #5 and #15 (Fig. 3**e–f**) reveal a large single pore object along with small pores which are distinctly different from the OM results. The limitation of each imaging technique is addressed in the last part of the result section.

The XCT results are used to classify three types of as-built samples: (1) Type I E-PBF samples, e.g. #8, containing mostly spherical pores that are randomly distributed in the core of the samples with $P < 1$ % (Fig. 3**a** and **d**); (2) Type II E-PBF samples containing a mixture of small pores and inter-connected pores with $1\ \% < P \leq 5\ \%$ (Fig. 3**b** and **e**); and (3) Type III E-PBF samples containing mainly inter-connected pores with $P > 5$ % (Fig. 3**c** and **f**).

Here, we further selected a region of interest at the core region of the 7 as-built samples and quantified the internal porosity (%), pore volume (*PV*), and pore surface area (*SA*) to elucidate their impact on the HIPped microstructure, see Fig. 4. In general, the *P*, *PV,* and *SA* increase when the energy density is low, especially when the processing parameters are at a combination of high SF (> 19) and high BF (Table 1 and Fig. 4**h**). We summarised key metrics from the XCT porosity analysis in Table 4 and they match well with the trend shown in Table 3.

Fig. 4**a–g** visualise three distinctive types of pore structures (depicted in Fig. 3) across 7 selected samples in 3D. These rendered images indicate the threshold parameters for the grain transition which can be used as a microstructure selection map for E-PBF/HIP Ti-6Al-4V. Fig. 4**a–b** show a 3D pore structure of Type I E-PBF samples, e.g. samples #1 and #8, which exhibit a low level of porosity. Given that the E-PBF operates in a vacuum but with a low helium pressure, these pores (Fig. 4**a**) are

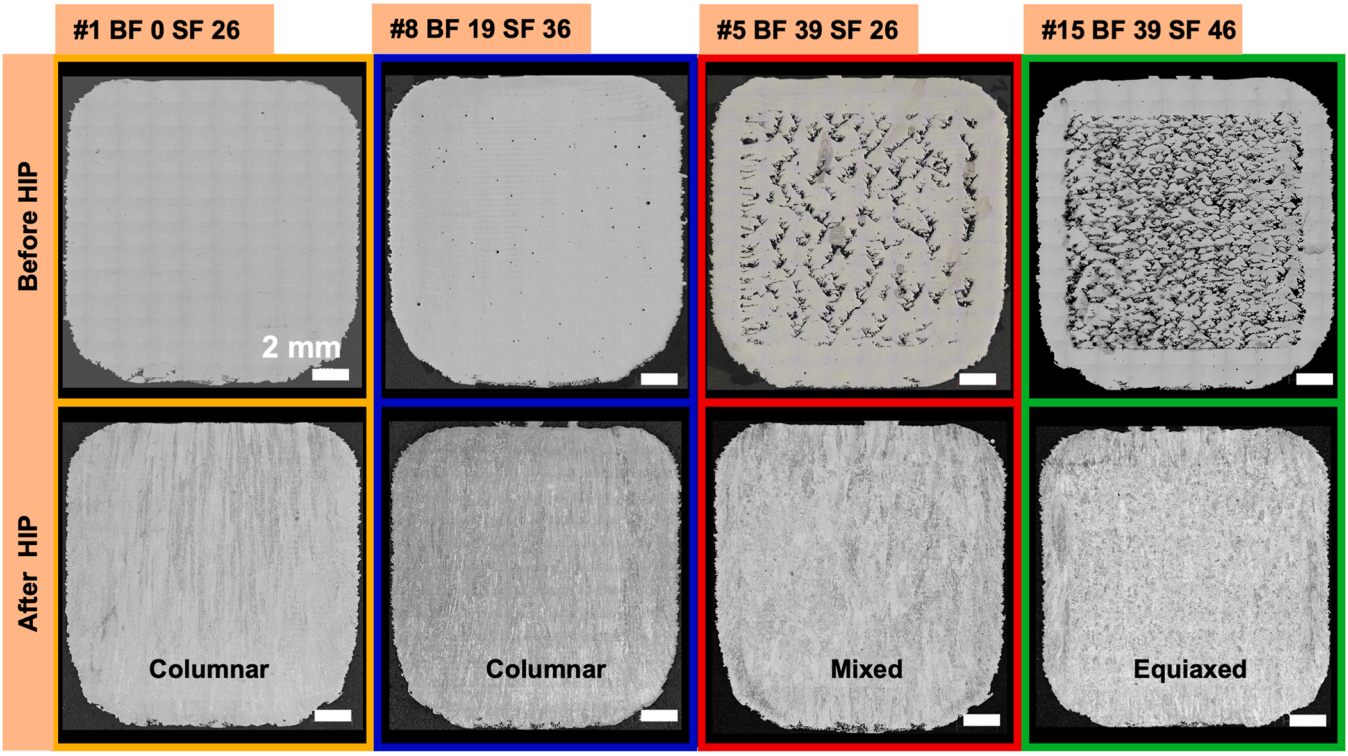

Fig. 2. Selected optical micrographs (OM) showing different types of porosity exhibited in the as-built samples, and the corresponding micrographs showing various types of grain microstructure after HIP. All scale bars are 2 mm.

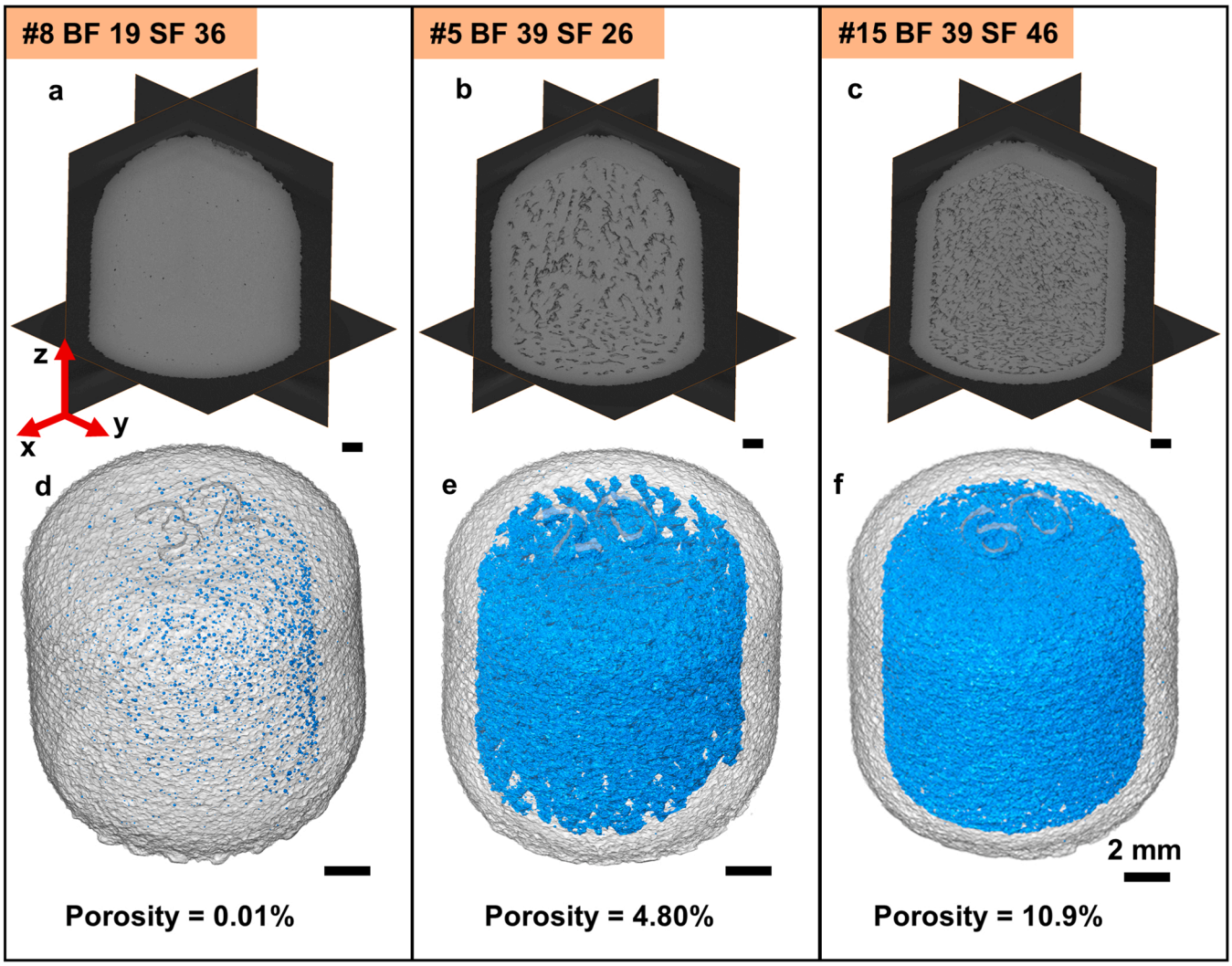

Fig. 3. 3D rendered images of three E-PBF as-built samples: (a–c) Orthoslices *x-y, x-z,* and *y-z* directions; and (d–f) show the internal features wherein the grey and blue objects represent Ti-6Al-4V material and porosity, respectively.

most likely to be the gas pores due to their small size and spherical shape which could be formed via pore transfer from powder to the melt pool during processing [25] (corroborate with the OM results in Fig. 2). The OM and XCT results confirm that these as-built samples are 99.9 % dense and suggest that their internal pores have negligible effects on the applied pressure during HIPping (quantified later).

For the Type II E-PBF samples (Fig. 4**c–e**), samples #9, #10, and #14 display a tortuous pore network along their build direction (e.g. Fig. 4**c**) and they contain small and randomly distributed gas pores (see examples in #10 and #14 Fig. 4**d–e**).

For the Type III E-PBF samples (Fig. 4**f–g**), samples #5 and #15, display a highly dense pore network with no preferred pore orientations. At a mid-high SF, the electron beam is defocussed and imposes a low energy density. This promotes the formation of lack-of-fusion defects [15,16,20] during E-PBF, resulting in un-melted regions at the core of the sample and forming a highly dense pore network with large surface areas. Although the sample geometry is similar for all processing themes, we hypothesis that the localised deformation at the core of specimens increases with increasing pore volumes, and the amount of deformation is expected to be the highest in Type III E-PBF samples, see discussion later.

3.3. The effects of pore morphology on plastic deformation during HIP

To confirm whether our samples underwent plastic deformation, we further estimated the applied pressure acting on the core region of E-PBF samples during HIP based on the OM porosity results. We assume the sample geometry is a cube and the area of the cubic face (A) is 15×15 mm^2. The applied force ($F_{applied} = P_{app} * A$) is estimated to be $\sim$ 23.2 kN at the HIP pressure of 103 MPa. We then calculated the local applied pressure at the core of each sample (P_{core}) by dividing $F_{applied}$ over the area of the core materials which is 12×12 mm^2 and the sample porosity (P, %) obtained from the OM images, see result summary in Table 5. We used the temperature-dependent mechanical properties of Ti-6Al-4V from [26] and a line of best fit to estimate the elastic limit or yield strength; $(\sigma_y) = -0.829(T) + 847.21$ ($r^2 = 0.989$), where the temperature (T) is 920 °C and hence the σ_y is $\sim$ 84.5 MPa. At this temperature, the P_{core} reaches up to 350 MPa, $\sim$ 4 times the σ_y of Ti-6Al-4V. This confirms that all samples underwent plastic deformation during HIP. Samples #15 and #16 underwent over 2.5 times the $\boldsymbol{\sigma_y}$ of Ti-6Al-4V at 920 °C, suggesting that dynamic recrystallisation may occur owing to hot deformation. On the other hand, the samples exhibit columnar and mixed microstructure when the applied pressure is < 2.1 and $2.1 < x < 2.7$ times the $\boldsymbol{\sigma_y}$ of Ti64 at 920 °C, respectively. During HIP, hot deformation is expected to be isotropic in samples #1 and #8 and much lower compared to samples #15 and #16.

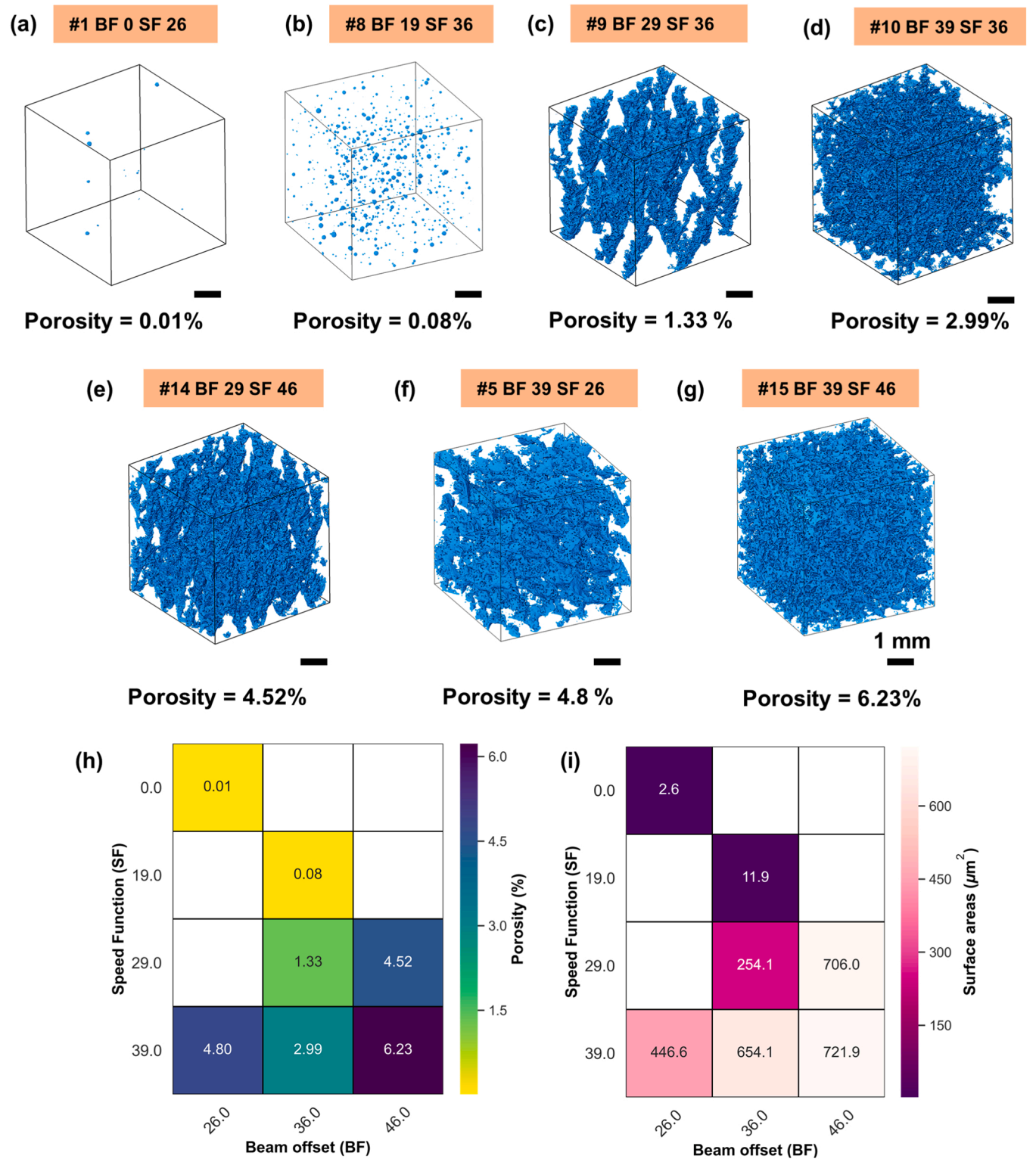

Fig. 4. 3D porosity analysis of E-PBF at the core of the as-built samples. All scale bars are in 1 mm. Region of interest 3D visualisation showing three distinctive pore morphologies; 'Type I – low level porosity': (a) #1 BF 0 SF 26; (b) #8 BF 19 SF 36; 'Type II – tortuous pore network': (c) #9 BF 29 SF 36; (d) #10 BF 39 SF 36; (e) #14 BF 29 and SF 46; 'Type III – highly dense pore network' (f) #5 BF 39 SF 26 and (g) #15 BF 39 SF 46. Summary plots showing their corresponding (h) porosity (%) and (i) surface areas.

Recrystallisation is a key driver to the formation of fine equiaxed microstructure. Prior work revealed that equiaxed structures were found in the region where large pores were present in the as-built AM sample [13,27–30] or/and the region underwent hot deformation, e.g. at the prior particle boundaries where the particles are in contact [31–33]. Given that our HIP temperature (920 °C) is within such crystallisation temperature range of Ti-6Al-4V (850 and 950 °C) [30], recrystallisation may occur during HIP. Recrystallisation was observed during HIP when the HIP temperature is below the transformation temperature of three types of Ti-alloys, e.g. Ti-6Al-4V [9,27–29], Ti10V2Fe3Al [34], and

Table 4
XCT quantification results for the core region of the as-built samples.

Sample #	BF	SF	Core porosity (%)	Shell porosity (%)	Total pore volume, *PV* (μm^3)	Total surface areas, *SA* (μm^2)	Grain microstructure after HIP
1	0	26	0.01	0.00	3.38×10^8	2.60×10^7	Columnar
8	19	36	0.08	0.03	2.61×10^9	1.19×10^8	Columnar
9	29	36	1.32	0.37	3.88×10^{10}	2.54×10^9	Columnar
10	39	36	3.01	0.74	8.65×10^{10}	6.54×10^9	Mixed
14	29	46	4.56	0.32	1.13×10^{11}	7.06×10^9	Mixed
5	39	26	4.80	0.02	1.10×10^{11}	4.47×10^9	Mixed
15	39	46	6.23	0.02	1.48×10^{11}	7.22×10^9	Equiaxed
16	–	–	7.27	0.55	1.79×10^{11}	7.60×10^9	Equiaxed

Table 5
Estimated applied pressure (P_{core}) on the core region of the E-PBF materials during HIP.

Sample #	$P_{core\ e}$ (MPa)	Multiples of Ti-6Al-4V σ_y (at 920 °C)	Microstructure
1	161	1.9	Columnar
8	161	1.9	Columnar
9	179	2.1	Columnar
10	196	2.3	Mixed
14	203	2.4	Mixed
5	189	2.2	Mixed
15	233	2.7	Equiaxed
16	350	4.1	Equiaxed

Ti48Al2Cr2Nb [35]. This suggests that the changes from columnar to equiaxed microstructure could be linked to the dynamic recrystallisation during HIP via hot deformation [36], and not due to the process itself.

Besides hot deformation, minimise the high-energy pore surfaces within the samples is another driving force for recrystallisation, which is the fundamental principle of HIP [37]. Bustillos et al. [9] explained that the stored energy associated with the pore surfaces is governed by the number of dislocations ahead of the defects or at the interphase boundaries, and the inherent strain energy associated with the non-equilibrium microstructure. E-PBF process relieves the accumulation of residual stress in the samples via preheating, this lowers inherent strain energy and is distinctively different from L-PBF process [9]. Results shown in Tables 4 and 5 suggest that the defects that might lead to recrystallisation of fine equiaxed grains but the as-built samples need to exhibit interconnected and tortuous pore with a large surface area rather than lack-of-fusion defects or porosities that are isolated from each other [9]. Our results also show that partially connected and directional defects will lead to a mixture of columnar and equiaxed grains.

Based on Tables 4 and 5, Figs. 2 **and** 4, we can see that the HIPped samples exhibited a fully columnar grain microstructure when the porosity level is at $P < 3$ % with mainly spherical micro-pores; a mixed grain microstructure of columnar and equiaxed when $3\ \% < P \leq 5\ \%$ and a tortuous and interconnected pore network appeared along the build direction; and an equiaxed grain microstructure when $P > 5$ % and a highly dense pore network existed with no preferred orientation.

We hypothesise that there may exist two main drivers for CET during HIP: (1) Increase in pore volume and surface area which promotes hot

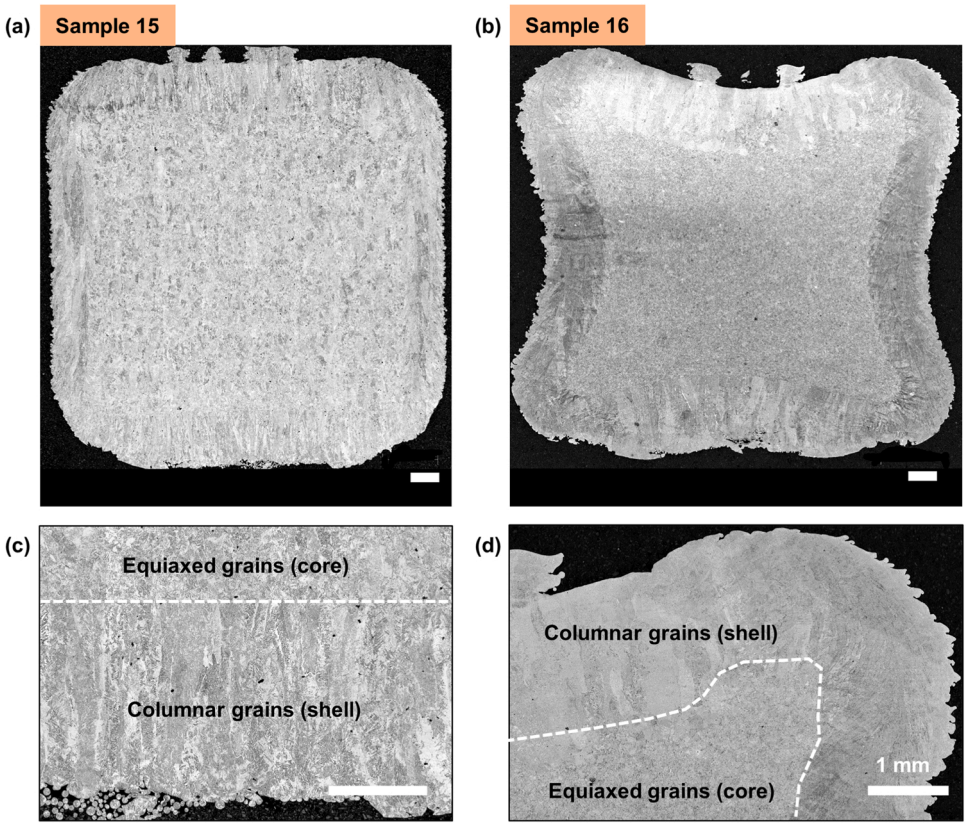

Fig. 5. OM microstructural images at X - Z sections of samples (a) #15 and (b) #16. (c–d) Enlarged views of shell and core microstructures for samples #15 and #16, respectively.

deformation at the core region of the samples and (2) minimise the high-energy pore surfaces within the samples.

3.4. Microstructural evolution after HIP Treatment

After the same HIP treatment, samples #15 and #16 (Fig. 5**a–b**) show a minimal amount of porosity ($P < 0.1$ %), equiaxed grain microstructure at the core region, columnar prior β grains, and dual-phase/Widmanstätten α/β microstructure at the shell, and an excellent bonding at the core-shell interface (Fig. 5**c–d**). The shell of sample #16 exhibited severely distorted columnar grains owing to the HIP-induced plastic deformation, underwent a shrinkage (~ 7.0 ± 0.1 %), and poor dimensional accuracy, and hence this setting is not recommended for future work.

The main difference between samples #15 and #16 is the core/shell microstructure in the as-built state (see Table 4). The core/shell materials in sample #15 were fully fused together before HIP and they have sufficient strength to withstand the applied pressure during HIP. The sample underwent isotropic compression and shrinkage (Fig. 5**a**). In contrast, the core/shell materials in sample #16 were weakly bonded together, however, the E-PBF melting and preheating effect sufficiently fused core/shell materials at the top and bottom part of the samples but not on the side wall. During HIP, the side wall of the sample was unable to withstand the HIP pressure and buckle, resulting in anisotropic compression (Fig. 5**b**). As the HIP cycle continued, the weakly bonded powder network at the sample core (formed by the preheating effect of E-PBF) broke down into individual powder particles. Upon additional pressure, the powder particles rotated to accommodate the plastic deformation. The porosity in the sintered network continued to reduce via typical creep mechanisms in the HIP treatment and eventually led to the formation of new grain boundaries and equiaxed grains (Fig. 5**c–d**). Our results further support that the key mechanism that drives the microstructural evolution is owing to the large pore volume and surface area in the as-built state, leading to large deformation and recrystallisation during HIP and the formation of equiaxed grains.

Unlike samples #15 and #16, the mixed type of microstructure is consistently observed in samples #14, #5, and #10 (Table 4), because the energy density was not enough to remelt previously built layers, forming residual voids in the core region. E-PBF/HIP can break up the columnar β-grains along the build direction, preventing the epitaxial grain growth using conventional PBF technologies [38]. A mixed microstructure is achieved in the post HIP samples, which could change the behaviour of crack propagations generated from the surface. Due to a nearly equiaxed structure, it tends to change direction on crack propagation, e.g. through the prior β grains. The closure of the voids during the HIP cycle also tends to break the α grain boundary for the columnar prior β grains, which may change the fatigue performance of the part. Seifi et al. [39] reported that heterogeneous microstructure in E-PBF samples shows no preferential paths during crack propagation, e.g. cracks were observed through α lath, colonies, and prior β grains across their test specimens.

Fig. 6 shows three investigated regions captured from samples #5, #8, and #15 before and after the HIP cycle. A finer α lath was observed before HIPping across all three samples and the HIP treatment increases the α lath width and hence the α colony scale factor [40]. Consequentially, this reduces the yield strength (YS) and ultimate tensile strength (UTS) but increases ductility [41].

Most of the as-built samples show an average α lath width of ~ 1 μm. Based on our results, the volumetric energy density delivered to the powder bed, resultant pore volume, and the cooling rate are critical factors for α lath width refinement. The HIPped cans had an increase in α lath width of ~ 200 %, similar to that reported by previous studies [40, 42]. There is a large deviation in the α lath width in the HIPped samples, which is a result of the range of phase transformations happening during heat treatment. This resultant α/β dual-phase microstructure is highly dependent on the α' martensitic formation and subsequent decomposition as well as the phase coarsening [43].

3.5. Mechanical properties

The micro-hardness at the core region of the as-built components is between 360 and 375 HV. It is slightly higher than the 340 HV measured by Kahlin et al. [44] but aligned with the Ref. [45]. Higher hardness is found on as-built samples with low porosity; this is potentially due to the rapid cooling achieved using less energy density in E-PBF. During the heating and cooling process, some differences in α and β formation were expected, with a consequent impact on prior β-grain width [19]. The effects of scanning speed and consequent volumetric energy density on

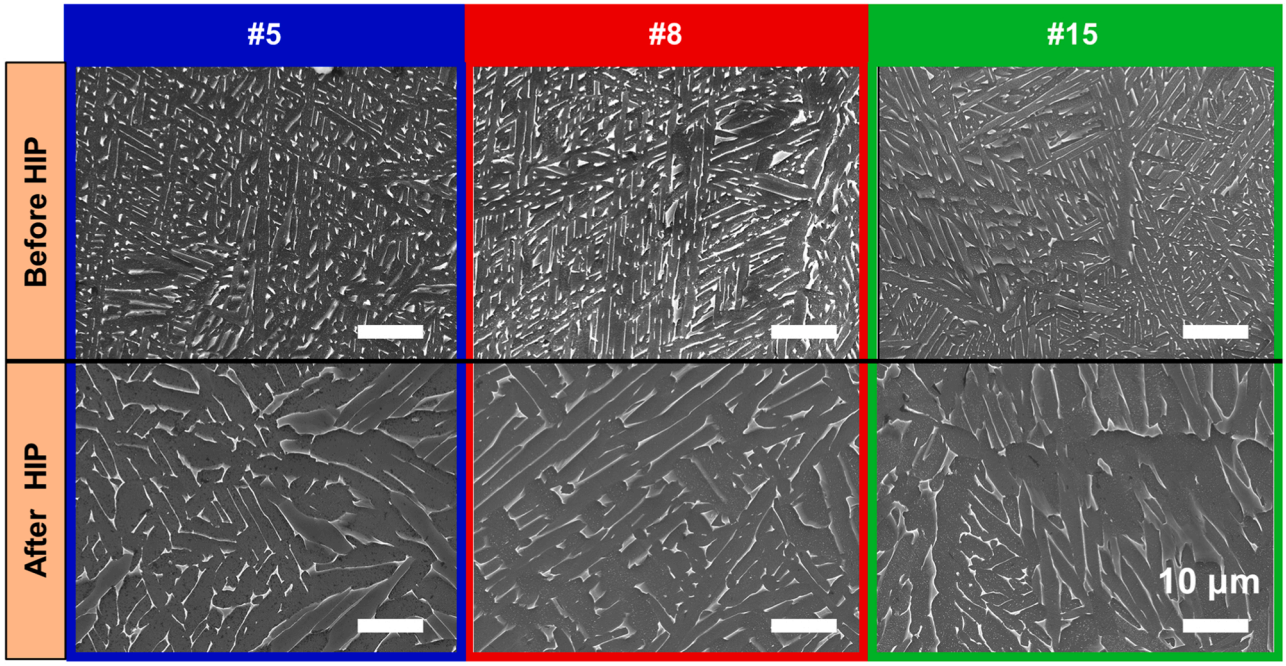

Fig. 6. The core microstructures of sample #5 (a–d), #8 (b–e), and #15 (c–f) before and after HIP treatment.

the mechanical properties are widely reported in the literature [19–21, 46]. The small variations (~ 4 %) in the micro-hardness results are influenced by the hardness measurement errors.

After HIP treatment, there is a slight decrease in micro-hardness which varies between 339 HV to 355 HV, similar to that reported by Ref. [47]. The difference in micro-hardness between the as-built and HIPped samples was < 5 %. Further work is required to fully understand the changes in hardness after HIP and their impact on the manufactured parts.

Fig. 7**a** shows a strong bonding at the core-shell interface, where the columnar prior β grains were observed in the E-PBFed region and equiaxed grains in the HIPed section. A surface fracture analysis was carried out on two of the tensile samples denoted as A and B (see Fig. 7**b** and **c**). Both samples show no lack of fusion or porosity and exhibit ductile behaviour indicated by the small dimples over the entire fracture surface. Sample A (Fig. 7**b**) shows fewer crack initiation sites at its surface than that of sample B (Fig. 7**c**) which has several spherical debonded particles at the inspected surfaces, which can act as stress raisers. After HIP, these tensile specimens with 0.18 wt% oxygen level exhibit ultimate tensile strength of 1019 ± 2 MPa, yield strength of 920

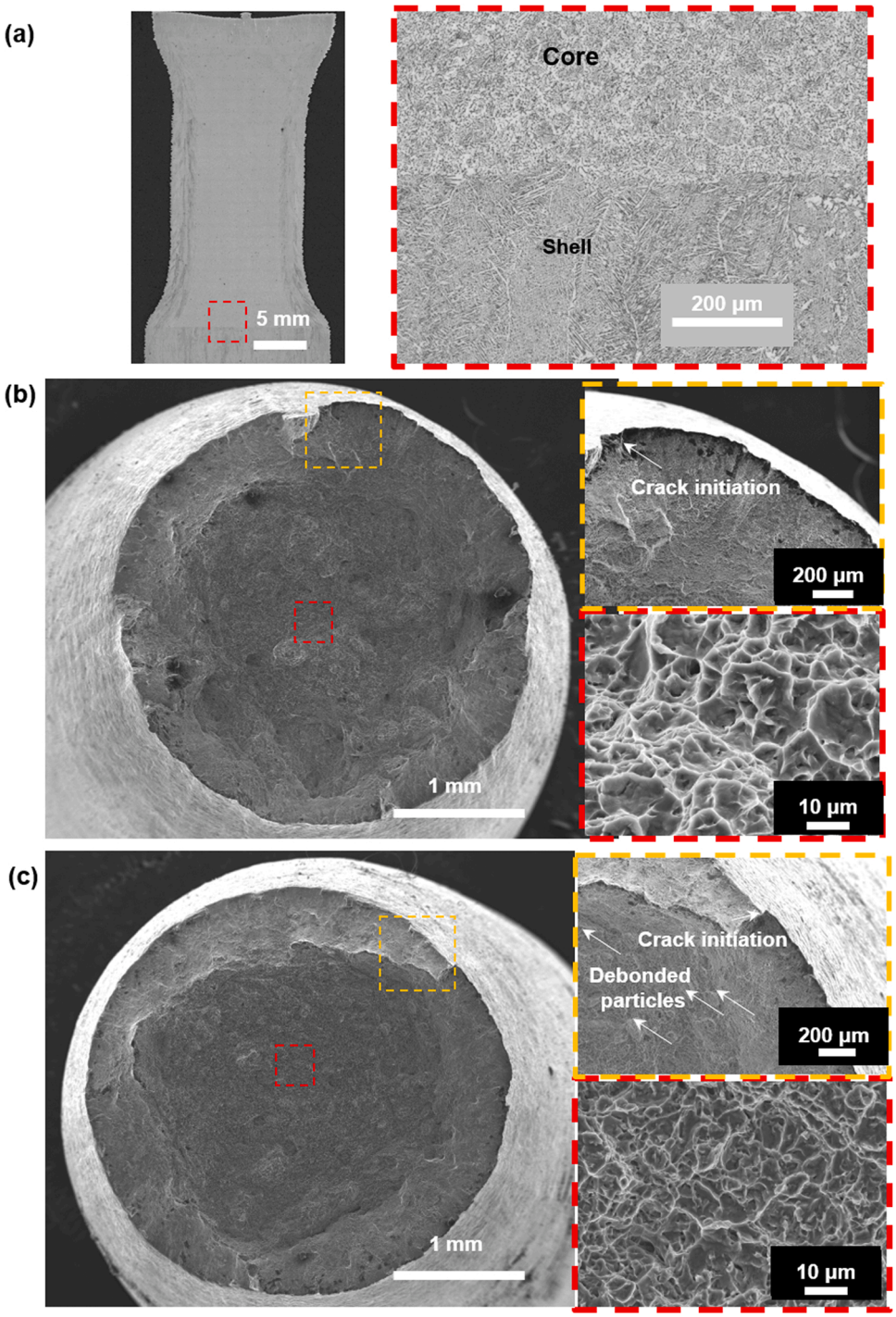

Fig. 7. (a) HIPped region of a tensile specimen before being machined with an enlarged view of the interface between core and shell regions. (b) SEM surface fracture of tensile sample A, with a crack initiation region, and its ductile fracture. (b) Tensile sample B surface fracture, with a crack initiation region and particles debonded, and its ductile fracture.

± 5 MPa, and elongation of 14.5 ± 2.0 %, which are slightly higher than the HIPped samples reported in ref [42,48,49] and the ASTM-F2924 standard [23,50]. The E-PBF/HIP technique can improve the ductility and fatigue properties of parts [12]. The difference in elongation (%) between samples A (16 %) and B (14 %) can be attributed to the oriented columnar grains in sample A along with the test direction. This result is comparable to the HIP sample with equiaxed grains which has an elongation of ~ 14 % [51].

3.6. Manufacturing efficiency analysis

Fig. 8 shows the run time of each melt theme and the corresponding sample porosity and density measured by OM and Archimedes tests, respectively. The porosity of these E-PBF samples quantified by XCT is significantly lower than that quantified by OM analysis because the XCT analysis quantifies the porosity of the entire can whereas the OM analysis only considers the core material. Each characterisation method has its possible sources of errors, e.g. the 2D OM images can underestimate a bulk sample density and they are not as representative as other measurements. The XCT analysis quantifies the pore volume in the core region in 3D but it may underestimate the porosity due to the large voxel size, and the Archimedes method can overestimate the porosity as it may trap air bubbles at the sample surface during measurements.

The shell of the sample was manufactured in ~ 10.5 min and it is subtracted from the total manufacturing time for hatching calculations. Samples #12, #13, and #14 were made with an SF of 46, (*or* a high scan speed) and have the lowest manufacturing time. When the SF was set below 46, the manufacturing time increased by at least 36 min. Our work shows that a BF between 9 and 19, and a SF between 36 and 46 generated the best time vs density, excluding sample #7. The BF and SF in sample #7 were considered as standard settings. Its hatching time was almost 45 % slower than that of sample #12. An adjustment of the parameters should be considered to improve the manufacturing time. A BF of 39 shows poor manufacturing speed and high porosity and this setting must not be used for manufacturing.

The shortest build time was achieved in making sample #16 in which the sample is only built with a shell, containing the loose powder. Free core melting could drastically reduce the manufacturing time and consolidation can solely rely on the HIP treatment. However, it exhibits a high volume shrinkage after HIP and an equiaxed microstructure, in contrast to the columnar β grains normally observed in PBF technologies. Further process optimisation can be done via simulation [6] which can be used to predict shrinkage and metallurgical composition of specimens.

4. Conclusions

We conducted a comprehensive study of E-PBF/HIP of Ti-6Al-4V samples to investigate the microstructural and mechanical properties as well as the manufacturing efficiency. Our results demonstrated a way to control the HIPed microstructure of these E-PBF/HIP samples by varying their volume percentage and morphology of lack-of-fusion pores in the as-built state with a single set of HIP parameters.

The HIPped microstructure underwent a transition from fully columnar to columnar-equiaxed mixed and then fully equiaxed grains. They exhibited a fully columnar grain microstructure when the porosity, $P < 3$ % with mainly spherical micro-pores; a mixed grain microstructure of columnar and equiaxed when 3 % $< P \leq 5$ % and a tortuous and interconnected pore network appeared along the build direction; and an equiaxed grain microstructure when $P > 5$ % and a highly dense pore network existed with no preferred orientation. Thus, two main drivers were suggested for the grain morphology transitions during HIP: (1) an increase in pore volume would increase the localised applied pressure at the core of the samples up to 4 times the flow stress of Ti-6Al-4V at 920 °C and (2) to minimise lack-of-fusion pores with high surface energies in the as-built state, resulting in dynamic recrystallisation during HIP and formation of equiaxed grains.

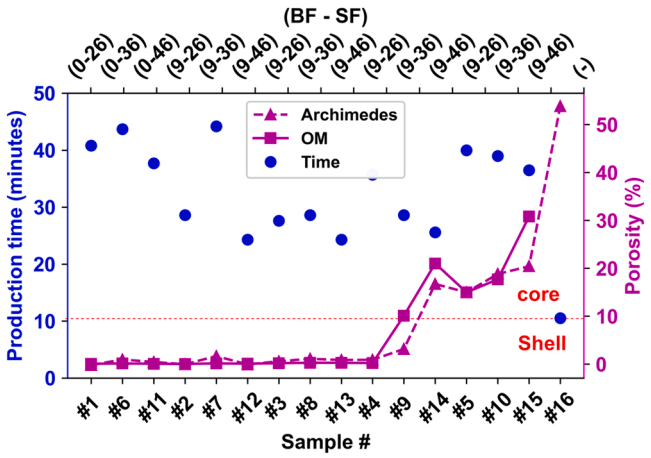

Fig. 8. Time vs shrinkage porosity of each condition manufactured.

The tensile testing results were above the ASTM-F2924 standard. The fracture surface shows a good bonding at the core-shell interface. Our results show that a BF between 9 and 19, and a SF between 36 and 46 generated the best outcome in terms of manufacturing time and quality. With further process optimisation, we believe that this E-PBF/HIP method can significantly reduce production time and manufacturing costs for E-PBF.

Author contribution

RT design the experiments and performed heat-treatment, mechanical tests, OM, and SEM. CLAL contributes to methodology, data analysis, XCT analysis, image-based modelling, and result interpretation. EM manufactured the parts; CLAL, TX, and RT led the paper writing, with all authors contributing.

CRediT authorship contribution statement

Emmanuel Muzangaza: Methodology. **Moataz M. Attallah:** Writing – review & editing, Supervision. **Chu Lun Alex Leung:** Writing – review & editing, Writing – original draft, Visualization, Software, Resources, Methodology, Investigation, Funding acquisition, Formal analysis, Data curation. **Xipeng Tan:** Writing – review & editing, Writing – original draft, Methodology. **Riccardo Tosi:** Writing – review & editing, Writing – original draft, Resources, Project administration, Methodology, Investigation, Formal analysis, Data curation, Conceptualization.

Declaration of Competing Interest

The authors declare that they have no known competing financial interests or personal relationships that could have appeared to influence the work reported in this paper.

Acknowledgement

CLAL is grateful for the support from MAPP: EPSRC Future Manufacturing Hub in Manufacture using Advanced Powder Processes (EP/P006566/1), EPSRC Impact Acceleration Account (EP/R511638/1), Manufacturing by Design (EP/W003333/1) and Made Smarter Innovation – Materials Made Smarter Research Centre (EP/V061798/1). RT and MMA acknowledge the Engineering Studentship by the MTC Engineering Doctorate Centre (EP/I017933/1).

References

[1] I. Gibson, D.W. Rosen, B.E. Stucker, D.B.S. Ian Gibson, David W. Rosen. Additive Manufacturing Technologies, 1st ed., Springer, New York, London, 2010.

[2] C. Körner, Additive manufacturing of metallic components by selective electron beam melting — a review, Int. Mater. Rev. 61 (2016) 361–377, https://doi.org/10.1080/09506608.2016.1176289.

[3] S. Tammas-Williams, P.J. Withers, I. Todd, P.B. Prangnell, The effectiveness of hot isostatic pressing for closing porosity in titanium parts manufactured by selective electron beam melting, Metall. Mater. Trans. A Phys. Metall. Mater. Sci. 47 (2016) 1939–1946, https://doi.org/10.1007/s11661-016-3429-3.

[4] A. du Plessis, S.M.J. Razavi, D. Wan, F. Berto, A. Imdaadulah, C. Beamer, J. Shipley, E. MacDonald, Fatigue performance of shelled additively manufactured parts subjected to hot isostatic pressing, Addit. Manuf. 51 (2022), 102607, https://doi.org/10.1016/j.addma.2022.102607.

[5] R. Knight, J. Wright, J. Beaman, D. Freitag, Metal processing using selective laser sintering and hot isostatic pressing (SLS/HIP), Proc. SFF Symp. (1996) 349–354, https://doi.org/10.15781/T22V2CW3Q.

[6] C. Qiu, N.J.E. Adkins, H. Hassanin, M.M. Attallah, K. Essa, In-situ shelling via selective laser melting: modelling and microstructural characterisation, Mater. Des. 87 (2015) 845–853, https://doi.org/10.1016/j.matdes.2015.08.091.

[7] M.A.N. Adkins, L. Carter, C. Qiu, K. Essa, Selective laser melting of components with thick section through in-situ shelling, in: Mater. Sci. Technol., Salt Lake City, 2016.

[8] H. Hassanin, K. Essa, C. Qiu, A.M. Abdelhafeez, N.J.E. Adkins, M.M. Attallah, Net-shape manufacturing using hybrid selective laser melting/hot isostatic pressing, Rapid Prototyp. J. 23 (2017) 720–726, https://doi.org/10.1108/RPJ-02-2016-0019.

[9] J. Bustillos, J. Kim, A. Moridi, Exploiting lack of fusion defects for microstructural engineering in additive manufacturing, Addit. Manuf. 48 (2021), 102399, https://doi.org/10.1016/j.addma.2021.102399.

[10] S. Riehm, V. Friederici, S. Wieland, Y. Deng, S. Herzog, A. Kaletsch, C. Broeckmann, Tailor-made functional composite components using additive manufacturing and hot isostatic pressing, vol. 64, 2021, pp. 295–307. ⟨https://doi.org/10.1080/00325899.2021.1901398⟩.

[11] A. Leicht, M.V. Sundaram, Y. Yao, E. Hryha, L. Nyborg, L.E. Rännar, A. Koptioug, K. Frisk, M. Ahlfors, As-HIP microstructure of EBM fabricated shell components, in: World PM 2016 Congr. Exhib., 2016. ⟨https://research.chalmers.se/en/publication/243463⟩, (Accessed 2 December 2021).

[12] K. Frisk, L.E. Rännar, A. Koptyug, N. Petterson, D. Persson, A. Leicht, M.V. Sundaram, E. Hryha, L. Nyborg, M. Ahlfors, Characterisation of EBM-built shelled samples of Ti6Al4V compacted by HIP, in: World PM 2016 Congr. Exhib., European Powder Metallurgy Association (EPMA), 2016. ⟨http://urn.kb.se/resolve?urn=urn:nbn:se:miun:diva-29742⟩, (Accessed 2 December 2021).

[13] E. Hernández-Nava, P. Mahoney, C.J. Smith, J. Donoghue, I. Todd, S. Tammas-Williams, Additive manufacturing titanium components with isotropic or graded properties by hybrid electron beam melting/hot isostatic pressing powder processing, Sci. Rep. 9 (2019) 1–11, https://doi.org/10.1038/s41598-019-40722-3.

[14] R. Tosi, Improving Productivity of an Electron Beam Melting System Using Ti-6Al-4V (EngD Thesis), Univ. Birmingham. Eng.D., 1988. ⟨https://ethos.bl.uk/OrderDetails.do?uin=uk.bl.ethos.837794⟩, (Accessed 9 May 2022).

[15] H. Gong, K. Rafi, T. Starr, B. Stucker, The effects of processing parameters on defect regularity in Ti-6Al-4V parts fabricated by selective laser melting and electron beam melting, in: Proceedings of the 24th Int. SFF Symp. – An Addit. Manuf. Conf. SFF 2013, 2013, pp. 424–39.

[16] C.L.A. Leung, R. Tosi, E. Muzangaza, S. Nonni, P.J. Withers, P.D. Lee, Effect of preheating on the thermal, microstructural and mechanical properties of selective electron beam melted Ti-6Al-4V components, Mater. Des. 174 (2019), 107792, https://doi.org/10.1016/j.matdes.2019.107792.

[17] T. Scharowsky, V. Juechter, R.F. Singer, C. Körner, Influence of the scanning strategy on the microstructure and mechanical properties in selective electron beam melting of Ti-6Al-4V, Adv. Eng. Mater. 17 (2015) 1573–1578, https://doi.org/10.1002/adem.201400542.

[18] N. Béraud, F. Vignat, F. Villeneuve, R. Dendievel, New trajectories in electron beam melting manufacturing to reduce curling effect, in: Procedia CIRP, Elsevier, 2014, pp. 738–743, https://doi.org/10.1016/j.procir.2014.02.038.

[19] S.P. Narra, R. Cunningham, J. Beuth, A.D. Rollett, Location specific solidification microstructure control in electron beam melting of Ti-6Al-4V, Addit. Manuf. 19 (2018) 160–166, https://doi.org/10.1016/j.addma.2017.10.003.

[20] H. Gong, K. Rafi, H. Gu, G.D. Janaki Ram, T. Starr, B. Stucker, Influence of defects on mechanical properties of Ti–6Al–4V components produced by selective laser melting and electron beam melting, Mater. Des. 86 (2015) 545–554, https://doi.org/10.1016/j.matdes.2015.07.147.

[21] H. Galarraga, R.J. Warren, D.A. Lados, R.R. Dehoff, M.M. Kirka, P. Nandwana, Effects of heat treatments on microstructure and properties of Ti-6Al-4V ELI alloy fabricated by electron beam melting (EBM), Mater. Sci. Eng. A 685 (2017) 417–428, https://doi.org/10.1016/j.msea.2017.01.019.

[22] A. Mohammad, A.M. Alahmari, M.K. Mohammed, R.K. Renganayagalu, K. Moiduddin, Effect of energy input on microstructure and mechanical properties of titanium aluminide alloy fabricated by the additive manufacturing process of electron beam melting, Materials 10 (2017), https://doi.org/10.3390/ma10020211.

[23] ASTM F3001-14, Standard specification for additive manufacturing titanium-6 aluminum-4 vanadium with powder bed fusion, ASTM Int., 2012, pp. 1–8. ⟨https://www.astm.org/f2924-14r21.html⟩, (Accessed 2 December 2021).

[24] S. Tammas-Williams, H. Zhao, F. Léonard, F. Derguti, I. Todd, P.B. Prangnell, XCT analysis of the influence of melt strategies on defect population in Ti-6Al-4V components manufactured by selective electron beam melting, Mater. Charact. 102 (2015) 47–61, https://doi.org/10.1016/j.matchar.2015.02.008.

[25] C.L.A. Leung, S. Marussi, R.C. Atwood, M. Towrie, P.J. Withers, P.D. Lee, In situ X-ray imaging of defect and molten pool dynamics in laser additive manufacturing, Nat. Commun. 9 (2018) 1355, https://doi.org/10.1038/s41467-018-03734-7.

[26] X. Lu, X. Lin, M. Chiumenti, M. Cervera, Y. Hu, X. Ji, L. Ma, H. Yang, W. Huang, Residual stress and distortion of rectangular and S-shaped Ti-6Al-4V parts by directed energy deposition: modelling and experimental calibration, Addit. Manuf. 26 (2019) 166–179, https://doi.org/10.1016/j.addma.2019.02.001.

[27] A. Abu-Issa, M. Lopez, C. Pickett, A. Escarcega, E. Arrieta, L.E. Murr, R.B. Wicker, M. Ahlfors, D. Godfrey, F. Medina, Effects of altered hot isostatic pressing treatments on the microstructures and mechanical performance of electron beam melted Ti-6Al-4V, J. Mater. Res. Technol. 9 (2020) 8735–8743, https://doi.org/10.1016/j.jmrt.2020.06.019.

[28] P. Li, D.H. Warner, J.W. Pegues, M.D. Roach, N. Shamsaei, N. Phan, Investigation of the mechanisms by which hot isostatic pressing improves the fatigue performance of powder bed fused Ti-6Al-4V, Int. J. Fatigue 120 (2019) 342–352, https://doi.org/10.1016/j.ijfatigue.2018.10.015.

[29] J. Benzing, N. Hrabe, T. Quinn, R. White, R. Rentz, M. Ahlfors, Hot isostatic pressing (HIP) to achieve isotropic microstructure and retain as-built strength in an additive manufacturing titanium alloy (Ti-6Al-4V), Mater. Lett. 257 (2019), https://doi.org/10.1016/j.matlet.2019.126690.

[30] M. Gushchina, G. Turichin, O. Klimova-Korsmik, K. Babkin, L. Maggeramova, Features of heat treatment the ti-6al-4v gtd blades manufactured by dld additive technology, Materials 14 (2021) 4159, https://doi.org/10.3390/ma14154159.

[31] C. Cai, B. Song, P. Xue, Q. Wei, J.M. Wu, W. Li, Y. Shi, Effect of hot isostatic pressing procedure on performance of Ti6Al4V: surface qualities, microstructure and mechanical properties, J. Alloy. Compd. 686 (2016) 55–63, https://doi.org/10.1016/j.jallcom.2016.05.280.

[32] K. Zhang, J. Mei, N. Wain, X. Wu, Effect of hot-isostatic-pressing parameters on the microstructure and properties of powder Ti-6Al-4V hot-isostatically-pressed samples, in: Metall. Mater. Trans. A Phys. Metall. Mater. Sci., Springer, 2010, pp. 1033–1045, https://doi.org/10.1007/s11661-009-0149-y.

[33] L. Xu, R. Guo, C. Bai, J. Lei, R. Yang, Effect of hot isostatic pressing conditions and cooling rate on microstructure and properties of Ti-6Al-4V alloy from atomized powder, J. Mater. Sci. Technol. 30 (2014) 1289–1295, https://doi.org/10.1016/j.jmst.2014.04.011.

[34] A.I. Dekhtyar, V.I. Bondarchuk, V.V. Nevdacha, A.V. Kotko, The effect of microstructure on porosity healing mechanism of powder near-β titanium alloys under hot isostatic pressing in α + β-region: Ti-10V–2Fe-3Al, Mater. Charact. 165 (2020), https://doi.org/10.1016/j.matchar.2020.110393.

[35] X. Yang, Z. Zhao, P. Bai, W. Du, S. Wang, EBSD investigation on the microstructure of Ti48Al2Cr2Nb alloy hot isostatic pressing formed by selective laser melting (SLM), Mater. Lett. 309 (2022), 131334, https://doi.org/10.1016/j.matlet.2021.131334.

[36] T. Furuhara, B. Poorganji, H. Abe, T. Maki, Dynamic recovery and recrystallization in titanium alloys by hot deformation, JOM 59 (2007) 64–67, https://doi.org/10.1007/s11837-007-0013-8.

[37] H.V. Atkinson, S. Davies, Fundamental aspects of hot isostatic pressing: an overview, Metall. Mater. Trans. A Phys. Metall. Mater. Sci. 31 (2000) 2981–3000, https://doi.org/10.1007/s11661-000-0078-2.

[38] Y. Kok, X.P. Tan, P. Wang, M.L.S. Nai, N.H. Loh, E. Liu, S.B. Tor, Anisotropy and heterogeneity of microstructure and mechanical properties in metal additive manufacturing: a critical review, Mater. Des. 139 (2018) 565–586, https://doi.org/10.1016/J.MATDES.2017.11.021.

[39] M. Seifi, A. Salem, D. Satko, J. Shaffer, J.J. Lewandowski, Defect distribution and microstructure heterogeneity effects on fracture resistance and fatigue behavior of EBM Ti–6Al–4V, Int. J. Fatigue 94 (2017) 263–287, https://doi.org/10.1016/j.ijfatigue.2016.06.001.

[40] S.S. Al-Bermani, M.L. Blackmore, W. Zhang, I. Todd, The origin of microstructural diversity, texture, and mechanical properties in electron beam melted Ti-6Al-4V, Metall. Mater. Trans. A Phys. Metall. Mater. Sci. 41 (2010) 3422–3434, https://doi.org/10.1007/s11661-010-0397-x.

[41] P. Homporová, C. Poletti, M. Stockinger, F. Warchomicka, Dynamic phase evolution in titanium alloy Ti-6A1–4V, in: Ti 2011 – Proc. 12th World Conf. Titan., Springer Verlag, 2012, pp. 737–40. ⟨https://doi.org/10.2/JQUERY.MIN.JS⟩.

[42] N. Hrabe, T. Gnäupel-Herold, T. Quinn, Fatigue properties of a titanium alloy (Ti–6Al–4V) fabricated via electron beam melting (EBM): effects of internal defects and residual stress, Int. J. Fatigue 94 (2017) 202–210, https://doi.org/10.1016/j.ijfatigue.2016.04.022.

[43] X. Tan, Y. Kok, Y.J. Tan, M. Descoins, D. Mangelinck, S.B. Tor, K.F. Leong, C. K. Chua, Graded microstructure and mechanical properties of additive manufactured Ti–6Al–4V via electron beam melting, Acta Mater. 97 (2015) 1–16.

[44] M. Kahlin, H. Ansell, J.J. Moverare, Fatigue behaviour of notched additive manufactured Ti6Al4V with as-built surfaces, Int. J. Fatigue 101 (2017) 51–60, https://doi.org/10.1016/j.ijfatigue.2017.04.009.

[45] N. Hrabe, T. Quinn, Effects of processing on microstructure and mechanical properties of a titanium alloy (Ti-6Al-4V) fabricated using electron beam melting (EBM), Part 2: energy input, orientation, and location, Mater. Sci. Eng. A 573 (2013) 271–277, https://doi.org/10.1016/j.msea.2013.02.065.

[46] P. Drescher, M. Sarhan, H. Seitz, An investigation of sintering parameters on titanium powder for electron beam melting processing optimization, Materials 9 (2016), https://doi.org/10.3390/ma9120974.

[47] S.S. Da Rocha, G.L. Adabo, G.E.P. Henriques, M.A.D.A. Nóbilo, Vickers hardness of cast commercially pure titanium and Ti-6Al-4V alloy submitted to heat treatments, Braz. Dent. J. 17 (2006) 126–129, https://doi.org/10.1590/s0103-64402006000200008.

[48] C. de Formanoir, S. Michotte, O. Rigo, L. Germain, S. Godet, Electron beam melted Ti-6Al-4V: microstructure, texture and mechanical behavior of the as-built and heat-treated material, Mater. Sci. Eng. A 652 (2016) 105–119, https://doi.org/10.1016/j.msea.2015.11.052.

[49] P. Li, D.H. Warner, A. Fatemi, N. Phan, Critical assessment of the fatigue performance of additively manufactured Ti-6Al-4V and perspective for future research, Int. J. Fatigue 85 (2016) 130–143, https://doi.org/10.1016/j.ijfatigue.2015.12.003.

[50] M.J. Donachie, Titanium: a technical guide, 2nd edition | Introduction to selection of titanium alloys, ASM Int. 180 (2000) 5–11.

[51] K. Zhang, Microstructure and Properties of HIPpd Powder Ti Alloys, Birminham Univ., 2010, pp. 1–266. ⟨http://etheses.bham.ac.uk/856/1/Zhang10PhD.pdf%5Cnpapers3://publication/uuid/439041F0-B2B7-44CC-B6AB-1517345C0703⟩, (Accessed 2 December 2021).